



# **Measuring the Muon Neutrino Magnetic Moment in the NOvA Near Detector**

Róbert Králik

*Supervisor:* Dr. Lily Asquith

*A thesis submitted in fulfilment of the requirements for the degree of  
Doctor of Philosophy to the*

School of Mathematical and Physical Sciences  
University of Sussex

In Brighton, United Kingdom

March 8, 2024

I hereby declare that I carried out this thesis independently, and only with the cited sources, literature and other professional sources.

I also declare that this thesis has not been and will not be, submitted in whole or in part to another University for the award of any other degree.

*Brighton, United Kingdom,*

*March 8, 2024*

---

Róbert Králik

# Acknowledgements

School of Mathematical and Physical Sciences, University of Sussex

DOCTORAL THESIS

---

Measuring the Muon Neutrino Magnetic Moment in the NOvA Near  
Detector

---

by Róbert Králik

**ABSTRACT**

Measuring an enhanced neutrino magnetic moment would be a clear indication of physics beyond the Standard Model (BSM), shedding light on the correct BSM theory or the potential Majorana nature of neutrinos. It would manifest in the NOvA near detector as an excess of neutrino-on-electron elastic scattering interactions at low electron recoil energies. Leveraging an intense and highly pure muon neutrino beam, along with the finely segmented liquid scintillator detector technology specifically designed for electromagnetic shower separation, enables NOvA to achieve a potentially world-leading sensitivity in probing the effective muon neutrino magnetic moment. Despite facing statistical limitations stemming from the low cross section of the signal process, systematic uncertainties have a significant impact on this result. To address these challenges, the NOvA Test Beam experiment focuses on mitigating some of the largest systematic uncertainties within NOvA by investigating particle interactions and energy deposition in a small-scale replica NOvA detector. This thesis describes the calibration of the NOvA Test Beam detector, which is a crucial step in analysing the Test Beam data before they can be utilised to reduce NOvA systematic uncertainties.

Keywords: neutrino NOvA electromagnetic testbeam calibration

# Contents

<b>Acknowledgements</b>	<b>ii</b>
<b>List of Figures</b>	<b>v</b>
<b>List of Tables</b>	<b>vi</b>
<b>1 The NOvA experiment</b>	<b>1</b>
1.1 The Neutrino Beam . . . . .	1
1.2 The NOvA Detectors . . . . .	4
1.3 Readout and Data Acquisition . . . . .	6
1.4 Simulation . . . . .	8
1.5 Data Processing and Event Reconstruction . . . . .	11
1.6 Detector Calibration . . . . .	11
1.6.1 Threshold and shielding correction . . . . .	15
1.6.2 Relative calibration . . . . .	16
1.6.3 Absolute calibration . . . . .	17
1.7 Systematic Uncertainties at NOvA . . . . .	18
1.7.1 Systematic Uncertainties Related to the NOvA Neutrino Beam	18
1.7.2 Systematic uncertainties for NOvA detectors . . . . .	19
<b>Glossary</b>	<b>20</b>
<b>Bibliography</b>	<b>21</b>

# List of Figures

1.1	The schematic of the NuMI beam facility . . . . .	2
1.2	NuMI neutrino beam components in the NOvA near detector . . . . .	3
1.3	The NOvA off-axis beam concept . . . . .	3
1.4	NOvA detectors . . . . .	4
1.5	NOvA Avalanche Photo Diodes . . . . .	6
1.6	NOvA Front End Board . . . . .	7
1.7	Illustration of the tricell condition (a). We only use hits that have two surrounding hits in the same plane to be used in the NOvA calibration. This is to ensure a good quality of the path length ( $d$ ) reconstruction, which is calculated from the known cell height ( $h$ ) and the reconstructed track angle ( $\varphi$ ). In case the hit is next to a bad channel (b), we ignore this bad channel and require a hit in the next cell over. . . . .	12
1.8	The Test Beam detector is (like the standard NOvA detectors) divided into 12 brightness bins (left plot), each representing a relative difference in energy response (right plot) due to different brightnesses of the fibres, scintillators, or readout. . . . .	14

# List of Tables

1.1	Models and tunes used in the NOvA simulation of neutrino interactions.	10
1.2	Definitions of variables commonly used in calibration [? ? ].	15

# CHAPTER 1

## The NOvA experiment

The NuMI Off-axis  $\nu_e$  Appearance (NOvA) experiment [1] is a long-baseline neutrino oscillation experiment based at the Fermi National Accelerator Laboratory (Fermilab) [2]. NOvA receives an off-axis  $\nu_\mu$  and  $\bar{\nu}_\mu$  beam from Fermilab's NuMI neutrino source, described in Sec. 1.1, and measures  $\nu_e/\bar{\nu}_e$  appearance and  $\nu_\mu/\bar{\nu}_\mu$  disappearance between its two highly active and finely segmented detectors, described in Sec. 1.4 [3].

The capability to measure both  $\nu_e$  and  $\bar{\nu}_e$  appearance, coupled with a significant matter effect induced by the long baseline, allows NOvA to address some of the most important questions in neutrino physics to date, such as the neutrino mass ordering, the octant of  $\theta_{23}$ , and the possible CP violation in the neutrino sector [3–7]. NOvA data also enables measurements of the values of  $\theta_{13}$ ,  $\theta_{23}$  and  $|\Delta m_{atm}^2|$  [3], measurements of neutrino differential cross sections in the near detector [8–11], constraints on the possible sterile neutrino models [12, 13], monitoring for supernova neutrino activity [14, 15], searches for magnetic monopoles [16], and constraints on the neutrino electromagnetic properties (this thesis). Using two functionally identical detectors mitigates the systematic uncertainties of neutrino oscillation measurements, described in Sec. 1.7.

NOvA started taking data in February 2014 and is expected to run through 2026 [17]. *TO DO: Add DUNE into this and find the LOI reference*

### 1.1 The Neutrino Beam

The neutrino beam for NOvA comes from the Fermilab-based *Neutrinos at the Main Injector* (NuMI) neutrino source [18]. The schematic description of NuMI is shown in Fig. 1.1, starting on the left hand side with 120 GeV protons from the Main Injector (MI), part of the Fermilab accelerator complex. The proton beam is divided into 10  $\mu$ s

long pulses, with  $\sim 5 \times 10^{13}$  protons on target (POT) per spill every  $\sim 1.3$  s long cycle time, resulting in a proton beam power of  $\sim 800$  kW, with upgrades currently underway to surpass 1 MW [19].

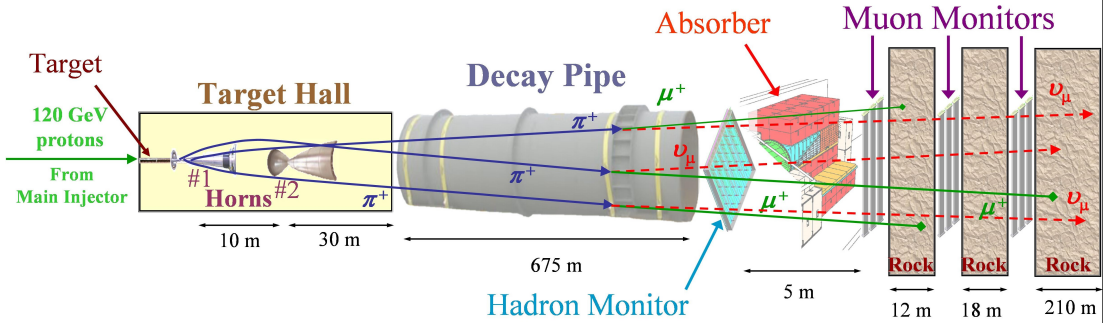


Figure 1.1: The NuMI neutrino beam starts on the left hand side with protons from the Main Injector impinged on a graphite target producing mainly pions and kaons. These are then focused and charge-selected by two focusing horns, after which they decay inside the decay pipe into a high-purity  $\nu_\mu$ , or  $\bar{\nu}_\mu$  beam. The residual hadrons are stopped and monitored in the hadron absorber and the remaining muons are recorded with muon monitors and absorbed inside the rock. Figure from [18].

The proton beam passes through a collimating baffle before hitting a  $\sim 1.2$  m-long (equal to about two interaction lengths) graphite target [20], producing hadrons, predominantly pions and kaons [18]. These are then focused and selected by two parabolic magnetic "horns". The focused hadrons pass through a 675 m-long decay pipe filled with helium to create a low density environment for hadrons to propagate and decay in flight into either neutrinos or antineutrinos. High energy hadrons that do not decay in the decay pipe are absorbed within a massive aluminium, steel, and concrete hadron absorber and monitored with a hadron monitor. The leftover muons are ranged out in dolomite rock after the absorber and monitored using three muon monitors. The hadron and all the muon monitors are ionization chambers, used to monitor the quality, location and relative intensity of the beam.

Using a positive current inside the horns focuses positively charged particles, which then decay into neutrinos, and removes negatively charged particles. Reversing the horn current focuses negatively charged particles, which decay into antineutrinos, and defocuses positively charged particles. The neutrino mode is therefore called Forward Horn Current (FHC) and the antineutrino mode is called Reverse Horn Current (RHC). The composition of the neutrino beam for both these modes at the NOvA near detector, shown as a rate of charged current events, is presented

in Fig. 1.2, displaying the very high purity  $\nu_\mu$  component in the FHC beam, and the high purity  $\bar{\nu}_\mu$  component in the RHC mode [18].

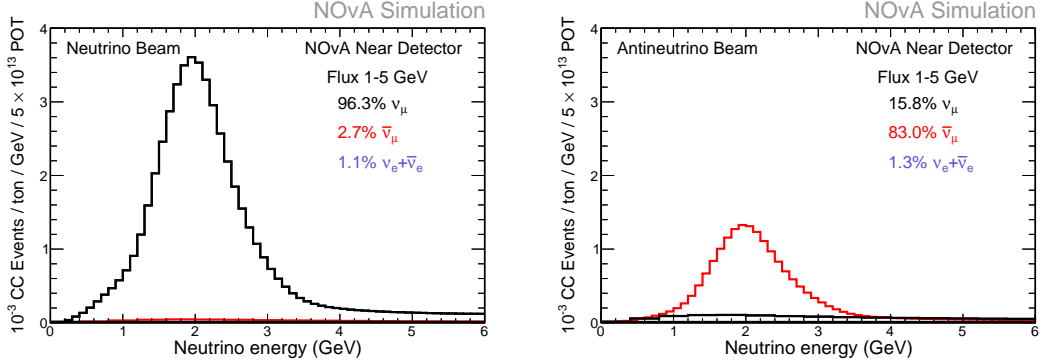


Figure 1.2: The charged current event rates for different neutrino flavours, as measured at the NOvA near detector in the FHC regime shown on the left, or the RHC regime on the right. The contribution of neutrino flavours to the event rates is also displayed, showing the high purity of the neutrino beam for NOvA. Figure from internal NOvA repository.

The resulting neutrino beam energy distribution is peaked at  $\sim 7$  GeV with a wide energy band. However, thanks to the kinematics of the dominant pion decay, by placing NOvA detector 14.6 mrad ( $\approx 0.8^\circ$ ) off the main NuMI beam axis, we achieve a narrow band neutrino flux peaked at 1.8 GeV [7, 21], as can be seen in Fig. 1.3. Using an off-axis neutrino flux increases the neutrino beam around 2 GeV about 5-fold compared to the on-axis flux and narrow-band peak enhances background rejection for the  $\nu_e$  appearance analysis [21].

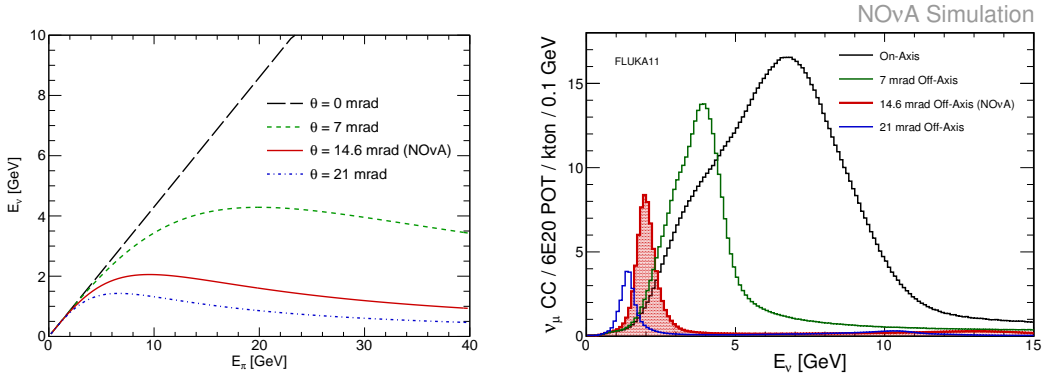


Figure 1.3: (Left) Dependence of the neutrino energy on the parent pion's energy and (right) neutrino energy distribution for an on-axis beam and three different off-axis beam designs. The case for NOvA is shown here in red and results in a narrow neutrino energy distribution around 2 GeV, with limited dependence on the parent pion's energy. Figure from [21]

## 1.2 The NOvA Detectors

The two main NOvA detectors are the Near Detector (ND), located in Fermilab  $\sim 1$  km from the NuMI target and  $\sim 100$  m under ground, and the Far Detector (FD), located  $\sim 810$  km from Fermilab at Ash River in north Minnesota, partially underground with a rock overburden [21]. NOvA also operated a detector prototype called Near Detector on the Surface (NDOS) used for early research and development of detector components and analysis [4]. Additionally, NOvA operated a Test Beam (TB) detector, described in detail in Sec. ???. The scale of ND and FD is shown in Fig. 1.4.

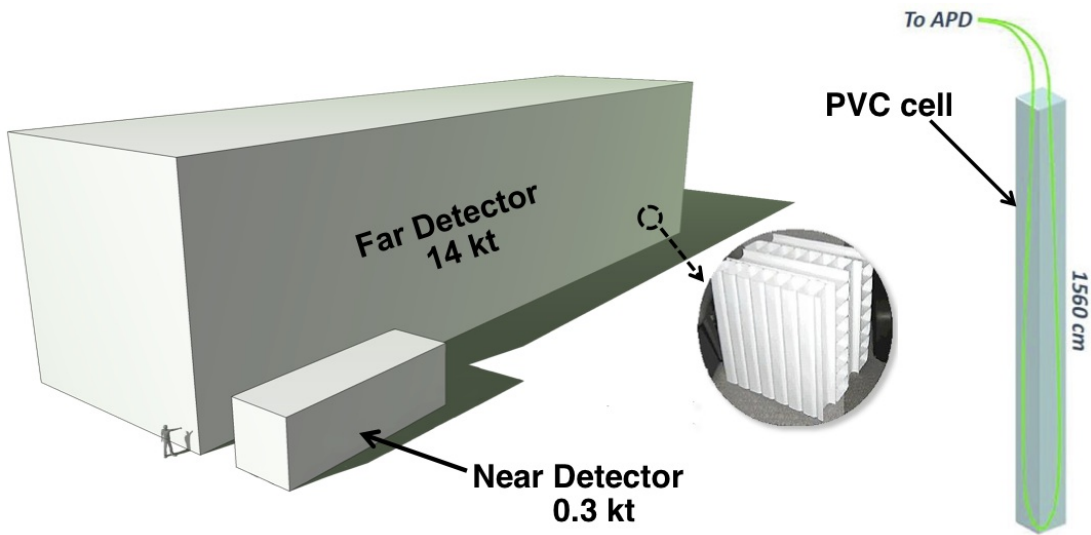


Figure 1.4: Schematic description of scale and composition of the NOvA detectors. The inset shows a photo of the orthogonal planes made out of PVC cells. An example of a far detector cell containing liquid scintillator and a loop of wavelength sifting fibre attached to an avalanche photodiode is shown on the right [22].

All NOvA detectors are highly segmented, highly active, functionally identical tracking calorimeters made up of polyvinyl chloride (PVC) cells filled with liquid scintillator. Each cell is a long rectangular cuboid with depth of 5.9 cm and width of 3.8 cm (with some variations), with cell length extending to the full width/height of each detector, which is  $\sim 4.1$  m for the ND and  $\sim 15.6$  m for the FD [21]. An example of a FD cell is shown on the right of Fig. 1.4.

Cells are connected side-by-side into a 16 cell-wide extrusions with 3.3 mm-wide walls between cells and 4.9 mm-wide walls on the outsides of the extrusions. The first and last cell of each extrusion are  $\sim 3$  mm narrower than the rest of the cells. Two extrusions are connected side-by-side to form a 32 cell-wide module, with each module

having a separate readout (see Sec. 1.3). In the FD, 12 modules are connected side-by-side to form one plane of the detector. In the ND only 3 modules make up a plane. Planes are positioned one after another, alternating between vertical and horizontal orientation, and grouped into diblocks, each containing 64 planes. The FD contains 14 diblocks, totalling 896 planes, whereas the ND contains 3 diblocks totalling 192 planes. However, the ND also consists of a Muon Catcher region, positioned right after the active region, consisting of 22 planes of the normal NOvA detector design, 2 modules high and 3 modules wide, sandwiched with 10 steel plates to help range out muons mainly from the  $\nu_\mu$  charged current interactions [4, 21].

Each cell is filled with a liquid scintillator consisting of mineral oil with 4.1% pseudocumene as the scintillant [23]. Each cell contains a single wavelength shifting fibre with double the length of the cell, looping at one end and connecting to the readout at the other. As light travels through the fibre, it is attenuated by about a fraction of ten for the FD cells **TO DO: Figure out what is the correct statement here.** The PVC walls of the detector cells are loaded with highly reflective titanium dioxide, with light typically bouncing off the PVC walls about 8 times before being captured by the fibre [21].

The final dimensions of the FD are  $15.6\text{ m} \times 15.6\text{ m} \times 60\text{ m}$  with a total mass of 14 kT and for the ND the dimensions are  $3.8\text{ m} \times 3.8\text{ m} \times 12.8\text{ m}$  with a mass of about 0.3 kT [17]. The active volume, consisting only of the liquid scintillator without the PVC structure, makes up about 70% of the total detector volume [21].

The NOvA detectors are specifically designed for electromagnetic shower identification, with a radiation length of 38 cm, which amounts to  $\sim 7$  planes for particles travelling perpendicular to the detector planes [4]. This is particularly useful to distinguish electrons and  $\pi^0$ s.

**TO DO: Talk here or in the next section about minimum electron energy to be recorded by NOvA detector and electronics. Maybe in all sections including reconstruction to tie them together**

### 1.3 Readout and Data Acquisition

The signal from the wavelength shifting (WLS) fibres is read out by an Avalanche Photodiode (APD), converting the scintillation light into electrical signal, with a high quantum efficiency of  $\sim 85\%$  and a gain of 100 [21]. An example APD is shown in Fig. 1.5. Both ends of each fibre are connected to one of the 32 pixels on the APD, with each APD reading out signal from one module. To maximise the signal to noise ratio, the APDs are cooled to  $-15^{\circ}\text{C}$  by a thermoelectric cooler, with heat carried away by a water cooling system.

The combination of the APD quantum efficiency and the light yield, determined by the PVC reflectivity and scintillator and WLS fibre response, result in a signal requirement of at least 20 photoelectrons in response to minimum ionizing radiation at the far end of the FD cell.

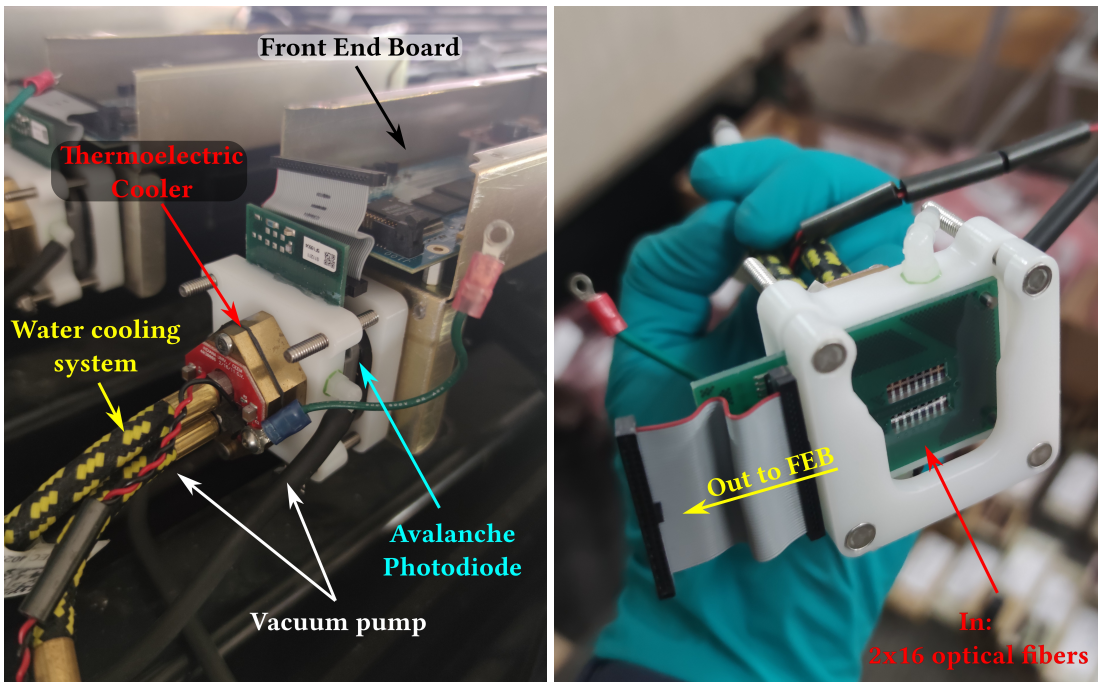


Figure 1.5: The modules with Avalanche Photo Diodes for NOvA mounted on top of the detector on the left picture, and shown from the bottom on the right. The individual components of the module are described. The left picture shows a disconnected ribbon cable and ground cable, which are normally connected to the front end board.

Each APD is connected to a single Front End Board (FEB), shown in Fig. 1.6. The FEB amplifies and integrates the APD signal, determines its amplitude and arrival time, before passing it to the data acquisition system (DAQ). On the FEB the APD signal is first passed to a custom NOvA Application-Specific Integrated Circuit (ASIC),

which is design to maximize the detector sensitivity to small signals. ASICs amplify, shape and combine the signal, before sending it to an Analog-to-Digital Converter (ADC). The combined noise from the APD and the amplifier is equivalent to about 4 photoelectrons, which, compared to an average photoelectron yield from the far end of the FD cell of 30, results in a good signal and noise separation [21]. The digitized data from an ADC is sent to a Field Programmable Gate Array (FPGA), which extracts the time and amplitude of the ADC signals, while subtracting noise based on a settable threshold. The FPGAs employ multiple correlated sampling methods to reduce noise and improve time resolution of the signal [24].

**TO DO:** *Find out what is the pedestal/threshold that's being subtracted*

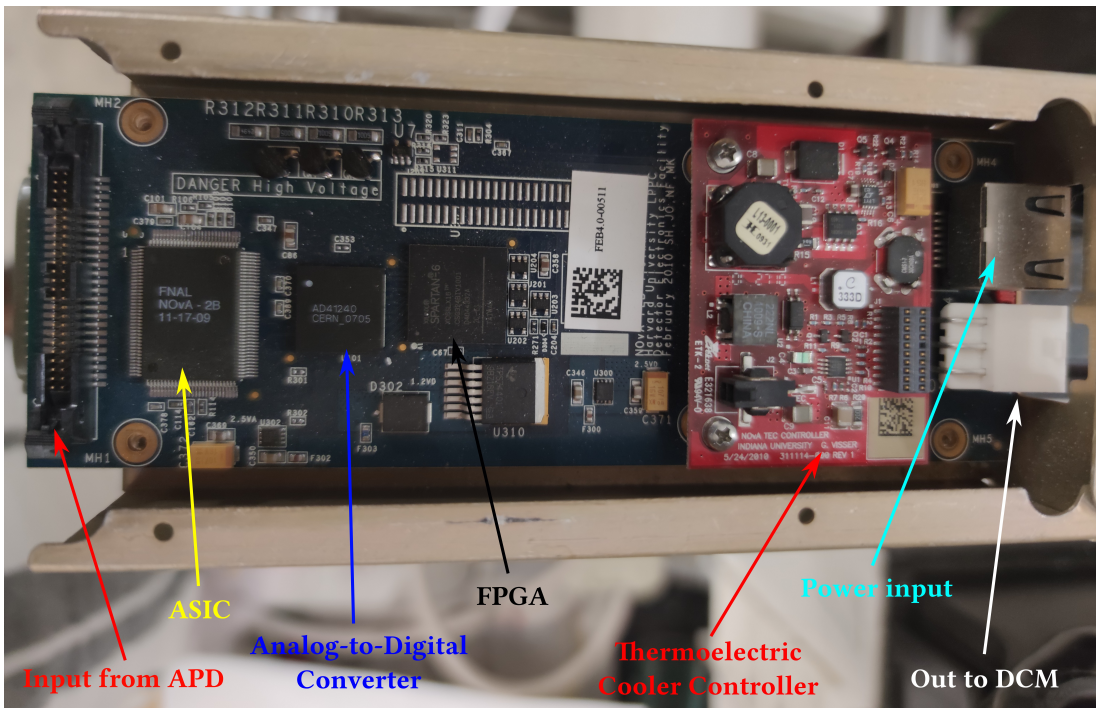


Figure 1.6: An example of a NOvA Front End Board with individual components labelled.

All of the NOvA front end electronics (APDs and FEBs) are operated in a continuous readout mode, without requiring any external triggers [21]. Due to higher detector activity during beam spills, the ND FEBs work at a higher frequency of 8 MHz, whereas the FD FEBs suffice with 2 MHz sampling frequency [24].

Data from up to 64 FEBs are concentrated in a Data Concentration Module (DCM), which concatenates and packages the data into 5 ms time slices, before sending it to the buffer nodes. DCMs are also connected to the timing system and pass a single

unified timing measurement to the FEBs to maintain synchronization across the detector [24].

The buffer nodes cache the data for at least 20 seconds while receiving information from the trigger system. Each trigger uses a time window based either on the time of the NuMI beam spill, on a periodic interval for readout of cosmic events for detector calibration and monitoring, or on a time of activity-based data-driven trigger [24]. Data that fall within any of the trigger windows are sent to a data logger system, where they are merged to form events, before being written to files for offline processing, or sent to an online monitoring system.

*COMMENT: Maybe talk about data quality as well? Probably should since I want to talk about good runs and bad channels in the TB calib chapter*

## 1.4 Simulation

*COMMENT: Should I divide the simulation into the individual stages? I had it like that originally, but for example the simulation of cosmics is only very short and not sure what section would I put it under*

To extract neutrino oscillation parameters, or to test a hypothesis, NOvA uses a series of simulations to make predictions according to various physical models [25]. The simulation chain can be divided into four parts: simulation of the neutrino beam, simulation of neutrino interactions within the NOvA detectors, simulation of cosmic particles interacting in the NOvA detector and simulation of the detector response.

To simulate the neutrino beam, NOvA uses the GEANT4 v9.2.p03 [26] based Monte Carlo (MC) simulation with a detailed model of the NuMI beamline [27], as it was described in Sec. 1.4. The simulation starts with MI protons interacting within the long carbon target and producing hadrons, mainly  $\pi$ ,  $K$  and  $p$ , followed by transport and possible further interaction of these hadrons within the focusing system, until finally ending with hadron decays producing the neutrino beam.

To account for the imprecise theoretical models used in GEANT4, we use the Package to Predict the Flux (PPFX) to incorporate external measurements of yields and cross sections of hadron production inside the target and other NuMI materials into the prediction [28]. The current version of PPFX is limited by the results available

during its creation and only corrects the most frequent interactions while assigning large systematics uncertainties to the rest (see Sec. 1.7). For the most common  $\pi$  production, PPFX uses the NA49 measurements [29] of 158 GeV/c protons interacting on a thin (few percent of interaction length) carbon target, with a few data point from Barton et al [30] to expand the kinematic coverage. These then have to be scaled to the 20 – 120 GeV/c incident proton energies seen in NOvA using the FLUKA [31, 32] MC generator. For the  $K$  production from  $p + C$  interaction, important for higher neutrino energies and electron neutrinos, PPFX uses the NA49  $K$  data [33] together with the NA49  $\pi$  data [29] multiplied by the  $K/\pi$  ratios of yields on thin carbon target from the MIPP experiment [34]. Lastly, for the nucleon production, PPFX uses the NA49 data on quasi elastic interactions [35]. All the other interactions inside NuMI, such as interaction in non-carbon targets, or interactions with hadrons other than protons, are either extrapolated from the previously mentioned measurements, or are not corrected for and a significant systematic uncertainty is assigned to them [28].

There's two new experiments that measured the production and interaction of hadrons on various targets and incident energies, specifically designed to improve the prediction of neutrino beams. I worked on implementing data from the NA61 experiment on hadron production from  $p + C$  interaction on a thin carbon target at 31 GeV/c [36], motivated by possible reduction in the  $K$  production systematic uncertainty. This work is still ongoing and will be implemented into PPFX and NOvA together with the rest of the NA61 measurement. The most impactful ones will be the measurement of hadron production from  $p + C$  interaction on a thin carbon target at 120 GeV/c [37] (no energy scaling required), measurements of  $p + C$  and  $p + Be$  at different incident energies [38],  $\pi + C$  and  $\pi + Be$  measurements at 60 GeV/c [39], resonance production measurements from 120 GeV/C  $p + C$  [40], and probably the most impactful one, the yet unpublished measurement of hadron production yield on a NOvA-era NuMI replica target at 120 GeV/c [41]. NA61 also measured the hadron production yield for the T2K experiment's replica target [42], which significantly reduced the neutrino flux systematic uncertainty for the T2K measurements [41]. The second experiment is EMPHATIC [43], which is currently analysing their data on a broad range of hadron production measurements, mainly the secondary and tertiary

interactions of various projectiles with a wide range of incident energies and thin target materials, complementary to the NA61 measurements.

*COMMENT: The description of neutrino interactions, including QE/Res/DIS scattering and nuclear effects will probably be in the theory chapter. If not I'll add it here.*  
*COMMENT: Might have to describe some of these interaction models a bit more if any of the cross section uncertainty for the magnetic moment analysis turns up to be significant*

The output of the neutrino beam simulation is passed to the simulation of neutrino interactions inside the detectors, which is done with the GENIE v3.0.6 [44] neutrino MC generator. GENIE allows users to choose the particular models for different types of neutrino interactions and particle propagation within the nucleus, as well as possible tunes to external measurements. The four main interaction modes in GENIE are the quasielastic charged current scattering (CCQE), the resonant baryon production (Res.), the deep-inelastic scattering (DIS), and the coherent pion production (COH $\pi$ ). Special case of CC interaction with two nucleons producing two holes via meson exchange currents (MEC) is also considered. Particles created in these processes are then propagated inside the nucleus according to the final state interaction model (FSI). All of these are set by the Comprehensive Model Configurations (CMCs) and NOvA currently uses the N1810j0000 CMC. Additionally, NOvA adds a tune to NOvA  $\nu_\mu$ CC data for the CCMEC interactions and a set of external  $\pi$  interaction measurements to constrain the FSI model. Table 1.1 shows the list of models and tunes for different interaction modes in NOvA [7].

Table 1.1: Models and tunes used in the NOvA simulation of neutrino interactions.

Interaction	Model	Tune
CCQE	València [45]	External $\nu$ – D data [46]
CCMEC	València [47, 48]	NOvA $\nu_\mu$ CC data
Res. & COH $\pi$	Berger-Sehgal [49, 50]	External $\nu$ – A data
DIS	Bodek-Yang [51, 52]	External $\nu$ – A data
FSI	Semi-classical cascade [53]	External $\pi$ – $^{12}$ C data

Since the FD is on the surface we also need to include a simulation of cosmic rays generated with the CRY [54] MC generator. The simulated cosmic muons are also used to calibrate NOvA detectors [28].

Particles that are created from neutrino interactions and cosmic rays are propa-

gated through the NOvA detectors using an updated version of GEANT4 v10.4.p02 [26]. The output of this simulation is the energy deposited in the scintillator, which is then passed to a custom NOvA simulation software [28]. The scintillation light generated by the deposited energy is parametrized using the Birks-Chou model [55], which corrects for recombination in organic scintillators at high deposited energies. The normalization factors for the produced scintillation light (the light yield), as well as for the Cherenkov light, which can affect the light readout, are tuned to NOvA cosmic data [9]. The light collection by the WLS fibres and its transport to the APDs, as well as the APD response use a parametrized simulation, which makes use of the fact that all the NOvA cells and their readout are generally the same across the detectors [28]. The simulation of the readout electronics is done by another custom NOvA parametrized model, which mainly account for a random electronics noise, with output in the same format as raw data.

Due to the high neutrino rate in the ND, there are neutrinos interacting in the surrounding rock creating particles that make it to the detector and act as background. To simulate these rock events we use the same simulation as for neutrino interactions inside the detector. However, since only a few particles make it into the detector, it would be very time consuming to run this simulation for every neutrino. Therefore, we create a separate simulation that includes the surrounding rock and then overlay the results into the normal NOvA simulation chain, which doesn't include the rock, so that the rate matches the NuMI neutrino rate [28].

## 1.5 Data Processing and Event Reconstruction

TO DO: *Write a basic description of the process from raw data to final predictions (or just caf's?)*

TO DO: *Reconstruction - describe the reconstruction tools used to get the final products, focusing on the electron reconstruction.*

## 1.6 Detector Calibration

TO DO: *Reorganize the calibration section, ideally make it much shorter and more concise*

The purpose of calibration is to make sure that we get the same amount of energy wherever or whenever it's deposited in whichever of NOvA's detectors and to express this amount of energy in physical units. The NOvA calibration uses cosmic ray muons, which provide a consistent, abundant, and well-understood source of energy deposition.

### Creating calibration samples

We want to select good quality cosmic ray muons. First, we remove beam related events based on their time stamps relative to the time of the beam spill. Next we apply reconstruction to get the CellHit, slicer, and track information, followed by a track-based selection to remove misreconstructed and poor quality events.

Since energy deposition depends on the path length particle travels through a cell, we only use hits for which we can reliably calculate their path length. We call these hits **tricell** hits, as we require that all accepted hits are accompanied by a recorded hit in both neighbouring cells of the same plane, as shown in Fig. 1.7. In case there is a bad channel in a neighbouring cell, we ignore this channel and look one cell further. We can then calculate the path length simply as the cell width divided by the cosine of the direction angle [? ? ].

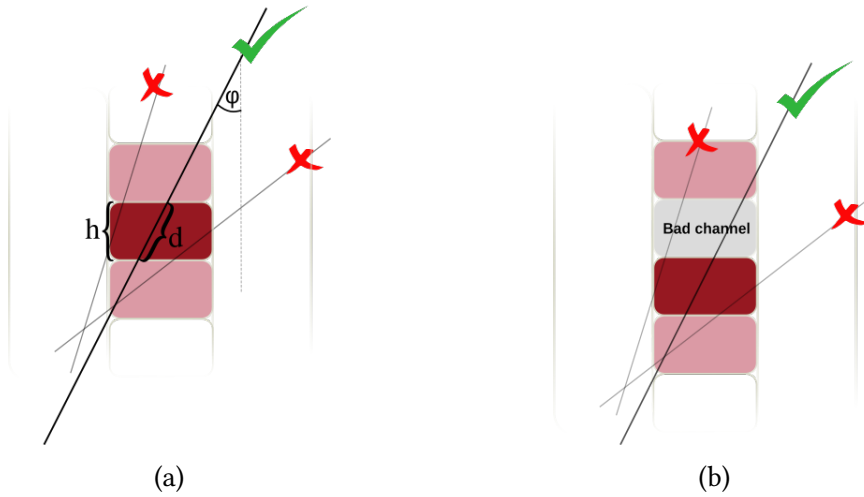


Figure 1.7: Illustration of the tricell condition (a). We only use hits that have two surrounding hits in the same plane to be used in the NOvA calibration. This is to ensure a good quality of the path length ( $d$ ) reconstruction, which is calculated from the known cell height ( $h$ ) and the reconstructed track angle ( $\varphi$ ). In case the hit is next to a bad channel (b), we ignore this bad channel and require a hit in the next cell over.

For the absolute calibration we select muons that stop inside the detector, by iden-

tifying muons with a Michel electron at the end of their track [? ].

For each data period or epoch and for each version of the simulation we create two calibration samples that are used as the input for the relative and absolute calibration. The samples are called [? ]

- `pclist` = **list** of **pre-calibrated hist**; Contains all selected cosmic muon events and is used in the relative calibration;
- `pcliststop` = `pclist` files only containing stopping muons used for the absolute calibration

### Fibre brightness

For data, the relative calibration is done for each individual cell in each plane to properly account for any potential variations, repeating the attenuation fit  $N_{cell} \times N_{plane}$  times. However, generating enough simulated events turned out to be computationally expensive. Therefore, assuming the simulated detector is approximately uniform plane to plane, for simulation we can "consolidate" the detector planes and only consider variations in the two views. Therefore for simulation we would repeat the fit  $N_{cell} \times N_{view}$  times [? ? ].

However, there are some variations in the detector response cell by cell that can be caused by different fibre brightnesses, but also by different qualities of the scintillator, air bubbles, APD gains, looped or zipped fibres and potentially others. We want to include these variations in the simulation to better match data. To emulate these differences in the simulation without the need to simulate every cell individually, we divide each detector into 12 brightness bins, as shown in Fig. 1.8. These brightness bins describe the relative differences in the detector response between individual cells [? ]. Therefore in the end, for simulation we perform the attenuation fit  $N_{cell} \times N_{view} \times N_{BrightnessBin}$  times.

To divide each detector into the 12 brightness bins, we use results from the relative calibration. Specifically we take the result of the attenuation fit (equal to the average response) in the centre of each cell to fill a 2D histogram. Then we normalize this histogram by dividing the response in each Cell  $\times$  View  $\times$  Plane by the average response in the corresponding Cell  $\times$  View. All uncalibrated cells get assigned the average response (1 in normalized histogram). Then we make a 1D histogram filled

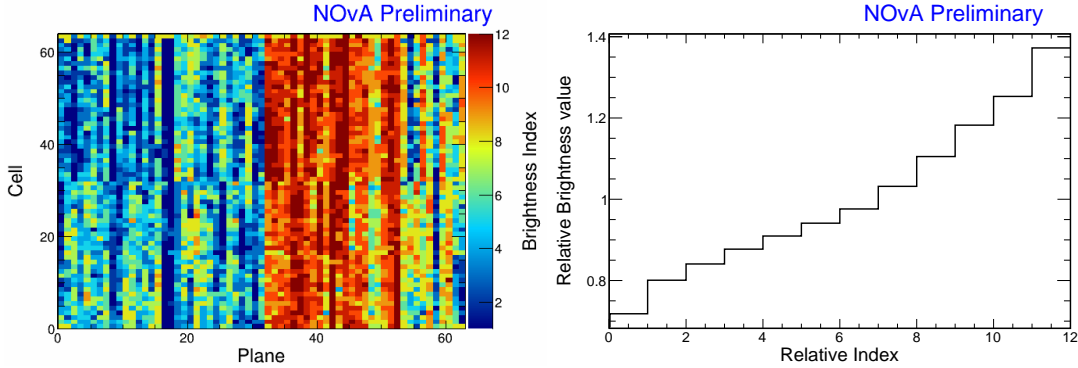


Figure 1.8: The Test Beam detector is (like the standard NOvA detectors) divided into 12 brightness bins (left plot), each representing a relative difference in energy response (right plot) due to different brightnesses of the fibres, scintillators, or readout.

with the normalized responses of each cell and divide this histogram into 12 equally populated bins (so each bin represents approximately the same number of detector cells, shown on the left plot of Fig. 1.8). The mean normalized response in each bin represents the relative brightness value of this bin (right plot of Fig. 1.8).

**TO DO:** *Describe the absolute and relative calibration just in text* The NOvA calibration consists of two parts [? ]:

1. The **relative calibration** corrects for attenuation of scintillator light as it travels through the cell to the readout, as well as for differences between detector cells. This correction is calculated for each cell separately.
2. Followed by the **absolute calibration**, which only uses stopping muons when they are minimum ionising particles. In the absolute calibration we calculate a scale between the measured energy deposition, corrected by the relative calibration, and the simulated energy deposition in physical units of MeV. This scale is calculated for each time period and each detector separately, which ensures the energy deposition is directly comparable wherever or whenever it occurred.

**TO DO:** *Just describe these units in text instead of here* The basic units and variables used to define energy deposited in the NOvA detectors are listed in table 1.2.

**TO DO:** *Change this equation to be simpler and also include T/S corrections* The final result of the NOvA calibration is the deposited energy in terms of physical units,

ADC	The digitized charge collected by the APDs from the Analog to Digital Converter [? ].
PE	Number of Photo Electrons. Calculated by a simple rescaling of the best estimate of the peak ADC. The PE per ADC scale only depends on the FEB type and the APD gain settings. This conversion is done before the calibration and PE serves as the base unit for calibration.
PECorr	<b>Corrected PE</b> after applying the relative calibration results. The correction is a ratio between an average energy response (a pre-determined semi-arbitrary number) and the result of the the relative calibration fit (also called attenuation fit), which depends on w, cell, plane, epoch and detector. This makes the energy response equivalent across each detector.
MEU	<b>Muon Energy Unit</b> is the mean detector response to a stopping cosmic minimum ionising muon. For true variables it's equivalent to the mean MeV/cm and for reconstructed variables to the mean PECorr/cm.
MeV	Estimated energy deposited in the scintillator calculated from PECorr using the results of the absolute calibration. Additional correction for dead material needs to be made in order to get an estimate of the calorimetric energy.

Table 1.2: Definitions of variables commonly used in calibration [? ? ].

which is in effect calculated as:

$$E_{dep}[\text{MeV}] = \underbrace{\frac{\text{MEU}_{truth}[\text{MeV}/\text{cm}]}{\text{MEU}_{reco}[\text{PECorr}/\text{cm}]}}_{\text{Absolute calibration}} \times \underbrace{\frac{\text{Average response}[\text{PECorr}]}{\text{Fitted response}[\text{PE}]}}_{\text{Relative calibration}} \times \underbrace{\left[ \frac{\text{PE}}{\text{ADC}} \right]}_{\text{Scale}} \times \text{Signal}[\text{ADC}],$$

(1.1)

where both the relative calibration results (blue fraction) and the absolute calibration results (red fraction) are stored in a database and applied together with the ADC-to-PE scale during processing of every hit in the NOvA detectors.

### 1.6.1 Threshold and shielding correction

Energy deposited far away from the readout may get attenuated enough to be shifted below the threshold. These low energy depositions would be missing from the attenuation fit, biasing it towards larger light levels with increasing distance from the readout. Similar effect, specifically for the vertical cells, is caused by using cosmic

muons for calibration and applying it to beam muons. The top of the detector effectively shields the bottom, skewing the energy distribution of cosmic muons. To correct for both of these effect, we use the simulation plist sample to calculate the threshold and shielding (also called threshold and shadowing) correction by comparing the true and reconstructed information. We apply this correction before the attenuation fits [? ].

### 1.6.2 Relative calibration

Relative calibration corrects for the attenuation of the scintillator light by fitting the average detector response over the position in each cell ( $w$ ), separately for every cell inside each detector. Dividing the "average response" of the detector by the result of the attenuation fit for each  $\text{Plane} \times \text{Cell} \times w$  combination effectively removes relative differences within and between all cells across the entire detector. The average response is a single constant number chosen to approximately represent the average response in the middle of the cell. Its value is for the far detector and Test Beam 39.91 PE/cm and for the near detector 37.51 PE/cm. The value of the average response has no impact of the calibration results, as the absolute scale of the detector response is determined during the absolute calibration and relative calibration only serves to remove the relative differences [? ? ].

To create the attenuation fit we use the following procedure [? ]:

1. Create the *attenuation profiles*. Attenuation profiles are essentially profile histograms of detector response in terms of PE/cm as a function of position in the cell ( $w$ ) for each cell in all planes. We construct the attenuation profiles over a little wider range than the actual length of the cell and always with 100 bins for each detector. This means that smaller detectors, like the Test Beam detector, have a finer binning ( $\sim 3\text{cm/bin}$ ) compared to the Far Detector ( $\sim 18\text{cm/bin}$ ).
2. Analyse the attenuation profiles. The job to create the attenuation profiles also creates validation histograms, which should be analysed prior to performing the attenuation fit to make sure the attenuation profiles look as expected.
3. Apply the threshold and shielding correction that was created before the relative calibration.

4. Do the attenuation fit over the full length of each cell. The fit consists of
  - (a) an exponential fit, which combines two cases. First, when the scintillating light travels the short distance straight to the readout, and second, when it goes to the far side of the cell and loops around before going to the readout. The fitted function has a form:
 
$$y = C + A \left( \exp\left(\frac{w}{X}\right) + \exp\left(-\frac{L+w}{X}\right) \right), \quad (1.2)$$
 where  $y$  is the fitted response,  $L$  is the length of the cell and  $C$ ,  $A$  and  $X$  are the fitted parameters.  $X$  also represents the attenuation length.
  - (b) Smoothing of the residuals from the exponential fit, mainly at the end of cells, with the LOcally WEighted Scatter plot Smoothing (LOWESS) method.
5. Check the plots of the attenuation fit for a selection of cells.
6. Save the fit result to the database in the form of two csv tables. The `calib_atten_consts.csv` table holds the results of the exponential fit, together with the final  $\chi^2$  of the fit. The `calib_atten_points.csv` table holds the results of the LOWESS smoothing.

To ensure the quality of the attenuation fit, we only apply the results if the final  $\chi^2 < 0.2$ . If  $\chi^2 > 0.2$ , we ignore the results for this cell and mark it as *uncalibrated*.

### 1.6.3 Absolute calibration

To find the absolute energy scale, we apply the relative calibration results on the stopping muon sample and look at the energy they deposited in cells 1-2 meters from the end of their tracks. In this track window they are approximately minimum ionising particles and their energy deposition is almost constant and well understood. Additionally, we don't use hits from the edges of a cell, as those might be affected by the lower number of events, fibre endings, or loops.

For each calibrated data and simulation sample we take a mean of the corrected deposited energy distribution, separate for each view. We then take a simple average from the two views to get the final  $\text{MEU}_{reco}$  in units of PECorr/cm for each sample

[? ]. Additionally, from simulation we can get the mean of the distribution of the true deposited energy in the scintillator,  $\text{MEU}_{truth}$  in units of MeV/cm for the same sample of stopping muons.

We ignore the energy that is lost in the dead material (PVC extrusions) and deal with it separately. The absolute energy scale for each sample is then the ratio of  $\text{MEU}_{truth}/\text{MEU}_{reco}$ . We save these absolute energy scales in another csv table called `calib_abs_consts.csv` which stores the MEU values and their errors.

As part of the absolute calibration we also produce validation plots that show the effect of calibration on the distribution of the stopping muons. We analyse these plots and if everything looks all right we load all the csv tables into the database.

## 1.7 Systematic Uncertainties at NOvA

TO DO: *Describe the general systematic uncertainties for NOvA* COMMENT: *These subsections below might end up just being paragraphs, depends how much I want to write about them*

### 1.7.1 Systematic Uncertainties Related to the NOvA Neutrino Beam

TO DO: *Describe the Hadron production and focusing systematic uncertainties*

TO DO: *Principal component analysis*

COMMENT: *Maybe briefly also mention the POT scaling normalization uncertainty.*

## Constraining the Hadron Production Systematic Uncertainty in NOvA

### 1.7.2 Systematic uncertainties for NOvA detectors

**Neutrino interaction systematic uncertainties**

**Energy scale systematic uncertainty**

**Cell edge calibration systematic uncertainty**

**Detector ageing systematic uncertainty**

COMMENT: *Should I include the neutron systematics, muon energy scale systematic, or tau scale systematics? Are these detector systematics? Should find out...*

# Glossary

**COMMENT:** *Should this be ordered by first appearance or alphabetically?*

CP	Charge conjugation Parity (symmetry)
NOvA	NuMI Off-axis $\nu_e$ Appearance (experiment)
NuMI	Neutrinos from the Main Injector
MI	Main Injector
POT	Protons On Target
FHC	Forward Horn Current (neutrino mode)
RHC	Reverse Horn Current (antineutrino mode)
ND	Near Detector
FD	Far Detector
NDOS	Near Detector on the Surface
TB	Test Beam
PVC	Polyvinyl chloride
WLS	Wavelength Shifting (fibre)
APD	Avalanche Photodiode
FEB	Front End Board
DAQ	Data Acquisition
ASIC	Application-Specific Integrated Circuit
ADC	Analog-to-Digital Converter
FPGA	Field Programmable Gate Array
DCM	Data Concentration Module
MC	Monte Carlo
PPFX	Package to Predict the Flux
CMC	Comprehensive Model Configuration

# Bibliography

- [1] Nova experiments official homepage. URL <https://novaexperiment.fnal.gov>. Cited February 2024.
- [2] Fermilab officail website homepage. URL <https://www.fnal.gov>. Cited February 2024.
- [3] Gary Feldman for the NOvA Collaboration. Physics of the nova experiment. White paper, 2012. URL <https://nova-docdb.fnal.gov/cgi-bin>ShowDocument?docid=7733>. Public NOvA document: NOVA-doc-7733-v1, cited on 05.2020.
- [4] R.B. Patterson. The NOvA Experiment: Status and Outlook. *Nucl. Phys. B Proc. Suppl.*, 235-236:151–157, 2013. doi:[10.1016/j.nuclphysbps.2013.04.005](https://doi.org/10.1016/j.nuclphysbps.2013.04.005).
- [5] P. Adamson et al. First measurement of muon-neutrino disappearance in NOvA. *Phys. Rev. D*, 93(5):051104, 2016. doi:[10.1103/PhysRevD.93.051104](https://doi.org/10.1103/PhysRevD.93.051104).
- [6] M.A. Acero et al. First Measurement of Neutrino Oscillation Parameters using Neutrinos and Antineutrinos by NOvA. *Phys. Rev. Lett.*, 123(15):151803, 2019. doi:[10.1103/PhysRevLett.123.151803](https://doi.org/10.1103/PhysRevLett.123.151803).
- [7] M. A. Acero et al. Improved measurement of neutrino oscillation parameters by the NOvA experiment. *Phys. Rev. D*, 106(3):032004, 2022. doi:[10.1103/PhysRevD.106.032004](https://doi.org/10.1103/PhysRevD.106.032004).
- [8] M. A. Acero et al. Measurement of neutrino-induced neutral-current coherent  $\pi^0$  production in the NOvA near detector. *Phys. Rev. D*, 102(1):012004, 2020. doi:[10.1103/PhysRevD.102.012004](https://doi.org/10.1103/PhysRevD.102.012004).
- [9] M. A. Acero et al. Measurement of the double-differential muon-neutrino charged-current inclusive cross section in the NOvA near detector. *Phys. Rev. D*, 107(5):052011, 2023. doi:[10.1103/PhysRevD.107.052011](https://doi.org/10.1103/PhysRevD.107.052011).
- [10] M. A. Acero et al. Measurement of the  $\nu_e$ –Nucleus Charged-Current Double-Differential Cross Section at  $\langle E_\nu \rangle = 2.4$  GeV using NOvA. *Phys. Rev. Lett.*, 130(5):051802, 2023. doi:[10.1103/PhysRevLett.130.051802](https://doi.org/10.1103/PhysRevLett.130.051802).

- [11] M. A. Acero et al. Measurement of  $\nu_\mu$  charged-current inclusive  $\pi^0$  production in the NOvA near detector. *Phys. Rev. D*, 107(11):112008, 2023. doi:[10.1103/PhysRevD.107.112008](https://doi.org/10.1103/PhysRevD.107.112008).
- [12] P. Adamson et al. Search for active-sterile neutrino mixing using neutral-current interactions in NOvA. *Phys. Rev. D*, 96(7):072006, 2017. doi:[10.1103/PhysRevD.96.072006](https://doi.org/10.1103/PhysRevD.96.072006).
- [13] M. A. Acero et al. Search for Active-Sterile Antineutrino Mixing Using Neutral-Current Interactions with the NOvA Experiment. *Phys. Rev. Lett.*, 127(20):201801, 2021. doi:[10.1103/PhysRevLett.127.201801](https://doi.org/10.1103/PhysRevLett.127.201801).
- [14] M. A. Acero et al. Supernova neutrino detection in NOvA. *JCAP*, 10:014, 2020. doi:[10.1088/1475-7516/2020/10/014](https://doi.org/10.1088/1475-7516/2020/10/014).
- [15] M. A. Acero et al. Extended search for supernovalike neutrinos in NOvA coincident with LIGO/Virgo detections. *Phys. Rev. D*, 104(6):063024, 2021. doi:[10.1103/PhysRevD.104.063024](https://doi.org/10.1103/PhysRevD.104.063024).
- [16] M. A. Acero et al. Search for slow magnetic monopoles with the NOvA detector on the surface. *Phys. Rev. D*, 103(1):012007, 2021. doi:[10.1103/PhysRevD.103.012007](https://doi.org/10.1103/PhysRevD.103.012007).
- [17] Peter N. Shanahan and Patricia LaVern Vahle. Physics with NOvA: a half-time review. *Eur. Phys. J. ST*, 230(24):4259–4273, 2021. doi:[10.1140/epjs/s11734-021-00285-9](https://doi.org/10.1140/epjs/s11734-021-00285-9).
- [18] P. Adamson et al. The NuMI Neutrino Beam. *Nucl. Instrum. Meth. A*, 806:279–306, 2016. doi:[10.1016/j.nima.2015.08.063](https://doi.org/10.1016/j.nima.2015.08.063).
- [19] Katsuya Yonehara. Megawatt upgrade of numi target system. 1 2022. URL <https://www.osti.gov/biblio/1844332>.
- [20] Leonidas Aliaga Soplin. *Neutrino Flux Prediction for the NuMI Beamline*. PhD thesis, William-Mary Coll., 2016.
- [21] D. S. Ayres et al. The nova technical design report. *NOvA Collaboration*, 2007. doi:[10.2172/935497](https://doi.org/10.2172/935497).

- [22] Yury Kudenko. Neutrino detectors for oscillation experiments. *JINST*, 12(06):C06003, 2017. doi:[10.1088/1748-0221/12/06/C06003](https://doi.org/10.1088/1748-0221/12/06/C06003).
- [23] S. Mufson et al. Liquid scintillator production for the NOvA experiment. *Nucl. Instrum. Meth. A*, 799:1–9, 2015. doi:[10.1016/j.nima.2015.07.026](https://doi.org/10.1016/j.nima.2015.07.026).
- [24] Xinchun Tian. NOvA Data Acquisition Software System. In *Meeting of the APS Division of Particles and Fields*, 9 2011.
- [25] A. Aurisano, C. Backhouse, R. Hatcher, N. Mayer, J. Musser, R. Patterson, R. Schroeter, and A. Sousa. The NOvA simulation chain. *J. Phys. Conf. Ser.*, 664(7):072002, 2015. doi:[10.1088/1742-6596/664/7/072002](https://doi.org/10.1088/1742-6596/664/7/072002).
- [26] S. Agostinelli et al. GEANT4—a simulation toolkit. *Nucl. Instrum. Meth. A*, 506:250–303, 2003. doi:[10.1016/S0168-9002\(03\)01368-8](https://doi.org/10.1016/S0168-9002(03)01368-8).
- [27] Zarko Pavlovic. *Observation of Disappearance of Muon Neutrinos in the NuMI Beam*. PhD thesis, Texas U., 2008.
- [28] L. Aliaga et al. Neutrino Flux Predictions for the NuMI Beam. *Phys. Rev. D*, 94(9):092005, 2016. doi:[10.1103/PhysRevD.94.092005](https://doi.org/10.1103/PhysRevD.94.092005). [Addendum: *Phys. Rev. D* 95, 039903 (2017)].
- [29] C. Alt et al. Inclusive production of charged pions in p+C collisions at 158-GeV/c beam momentum. *Eur. Phys. J. C*, 49:897–917, 2007. doi:[10.1140/epjc/s10052-006-0165-7](https://doi.org/10.1140/epjc/s10052-006-0165-7).
- [30] D. S. Barton et al. Experimental study of the  $a$  dependence of inclusive hadron fragmentation. *Phys. Rev. D*, 27:2580–2599, Jun 1983. doi:[10.1103/PhysRevD.27.2580](https://doi.org/10.1103/PhysRevD.27.2580).
- [31] T.T. Böhlen, F. Cerutti, M.P.W. Chin, A. Fassò, A. Ferrari, P.G. Ortega, A. Mairani, P.R. Sala, G. Smirnov, and V. Vlachoudis. The fluka code: Developments and challenges for high energy and medical applications. 120:211–214. ISSN 0090-3752. doi:[10.1016/j.nds.2014.07.049](https://doi.org/10.1016/j.nds.2014.07.049).
- [32] Alfredo Ferrari, Paola R. Sala, Alberto Fasso, and Johannes Ranft. FLUKA: A multi-particle transport code (Program version 2005). 10 2005. doi:[10.2172/877507](https://doi.org/10.2172/877507).

- [33] Gemma Maria Tinti. *Sterile neutrino oscillations in MINOS and hadron production in pC collisions*. PhD thesis, 2010.
- [34] Andrey V. Lebedev. *Ratio of Pion Kaon Production in Proton Carbon Interactions*. PhD thesis, 2007.
- [35] B Baatar, G Barr, J Bartke, L Betev, O Chvala, J Dolejsi, V Eckardt, HG Fischer, Z Fodor, A Karev, et al. Inclusive production of protons, anti-protons, neutrons, deuterons and tritons in p+ c collisions at 158 gev/c beam momentum. *The European Physical Journal C*, 73:1–66, 2013. doi:[10.1140/epjc/s10052-013-2364-3](https://doi.org/10.1140/epjc/s10052-013-2364-3).
- [36] N. Abgrall et al. Measurements of  $\pi^\pm$ ,  $K^\pm$ ,  $K_S^0$ ,  $\Lambda$  and proton production in proton–carbon interactions at 31 GeV/c with the NA61/SHINE spectrometer at the CERN SPS. *Eur. Phys. J. C*, 76(2):84, 2016. doi:[10.1140/epjc/s10052-016-3898-y](https://doi.org/10.1140/epjc/s10052-016-3898-y).
- [37] H. Adhikary et al. Measurements of  $\pi^+$ ,  $\pi^-$ ,  $p$ ,  $\bar{p}$ ,  $K^+$  and  $K^-$  production in 120 GeV/c p + C interactions. *Phys. Rev. D*, 108:072013, 2023. doi:[10.1103/PhysRevD.108.072013](https://doi.org/10.1103/PhysRevD.108.072013).
- [38] A. Aduszkiewicz et al. Measurements of production and inelastic cross sections for p+C , p+Be , and p+Al at 60 GeV/c and p+C and p+Be at 120 GeV/c. *Phys. Rev. D*, 100(11):112001, 2019. doi:[10.1103/PhysRevD.100.112001](https://doi.org/10.1103/PhysRevD.100.112001).
- [39] A. Aduszkiewicz et al. Measurements of hadron production in  $\pi^+ + C$  and  $\pi^+ + Be$  interactions at 60 GeV/c. *Phys. Rev. D*, 100(11):112004, 2019. doi:[10.1103/PhysRevD.100.112004](https://doi.org/10.1103/PhysRevD.100.112004).
- [40] H. Adhikary et al. Measurements of KS0,  $\Lambda$ , and  $\Lambda^-$  production in 120 GeV/c p+C interactions. *Phys. Rev. D*, 107(7):072004, 2023. doi:[10.1103/PhysRevD.107.072004](https://doi.org/10.1103/PhysRevD.107.072004).
- [41] Matej Pavlin. Hadron production measurements for neutrino experiments, 2020. URL [https://indico.fnal.gov/event/43209/contributions/187869/attachments/130502/159028/HadronProduction\\_neutrino2020.pdf](https://indico.fnal.gov/event/43209/contributions/187869/attachments/130502/159028/HadronProduction_neutrino2020.pdf). Presented on Neutrino 2020 conference.

- [42] N. Abgrall et al. Measurements of  $\pi^\pm$ ,  $K^\pm$  and proton double differential yields from the surface of the T2K replica target for incoming 31 GeV/c protons with the NA61/SHINE spectrometer at the CERN SPS. *Eur. Phys. J. C*, 79(2):100, 2019. doi:[10.1140/epjc/s10052-019-6583-0](https://doi.org/10.1140/epjc/s10052-019-6583-0).
- [43] T. Akaishi et al. EMPHATIC: A Proposed Experiment to Measure Hadron Scattering and Production Cross Sections for Improved Neutrino Flux Predictions. 12 2019.
- [44] C. Andreopoulos et al. The GENIE Neutrino Monte Carlo Generator. *Nucl. Instrum. Meth. A*, 614:87–104, 2010. doi:[10.1016/j.nima.2009.12.009](https://doi.org/10.1016/j.nima.2009.12.009).
- [45] J. Nieves, J. E. Amaro, and M. Valverde. Inclusive quasielastic charged-current neutrino-nucleus reactions. *Phys. Rev. C*, 70:055503, Nov 2004. doi:[10.1103/PhysRevC.70.055503](https://doi.org/10.1103/PhysRevC.70.055503).
- [46] Aaron S. Meyer, Minerba Betancourt, Richard Gran, and Richard J. Hill. Deuterium target data for precision neutrino-nucleus cross sections. *Phys. Rev. D*, 93:113015, Jun 2016. doi:[10.1103/PhysRevD.93.113015](https://doi.org/10.1103/PhysRevD.93.113015).
- [47] J. Nieves, I. Ruiz Simo, and M. J. Vicente Vacas. Inclusive charged-current neutrino-nucleus reactions. *Phys. Rev. C*, 83:045501, Apr 2011. doi:[10.1103/PhysRevC.83.045501](https://doi.org/10.1103/PhysRevC.83.045501).
- [48] R. Gran, J. Nieves, F. Sanchez, and M. J. Vicente Vacas. Neutrino-nucleus quasi-elastic and 2p2h interactions up to 10 gev. *Phys. Rev. D*, 88:113007, Dec 2013. doi:[10.1103/PhysRevD.88.113007](https://doi.org/10.1103/PhysRevD.88.113007).
- [49] Ch. Berger and L. M. Sehgal. Lepton mass effects in single pion production by neutrinos. *Phys. Rev. D*, 76:113004, Dec 2007. doi:[10.1103/PhysRevD.76.113004](https://doi.org/10.1103/PhysRevD.76.113004).
- [50] Ch. Berger and L. M. Sehgal. Partially conserved axial vector current and coherent pion production by low energy neutrinos. *Phys. Rev. D*, 79:053003, Mar 2009. doi:[10.1103/PhysRevD.79.053003](https://doi.org/10.1103/PhysRevD.79.053003).
- [51] A Bodek and U. K. Yang. Higher twist, xi(omega) scaling, and effective LO PDFs for lepton scattering in the few GeV region. *J. Phys. G*, 29:1899–1906, 2003. doi:[10.1088/0954-3899/29/8/369](https://doi.org/10.1088/0954-3899/29/8/369).

- [52] T. Yang, C. Andreopoulos, H. Gallagher, K. Hoffmann, and P. Kehayias. A Hadronization Model for Few-GeV Neutrino Interactions. *Eur. Phys. J. C*, 63: 1–10, 2009. doi:[10.1140/epjc/s10052-009-1094-z](https://doi.org/10.1140/epjc/s10052-009-1094-z).
- [53] L.L. Salcedo, E. Oset, M.J. Vicente-Vacas, and C. Garcia-Recio. Computer simulation of inclusive pion nuclear reactions. 484(3):557–592. ISSN 0375-9474. doi:[10.1016/0375-9474\(88\)90310-7](https://doi.org/10.1016/0375-9474(88)90310-7).
- [54] Chris Hagmann, David Lange, and Douglas Wright. Cosmic-ray shower generator (cry) for monte carlo transport codes. volume 2, pages 1143 – 1146. ISBN 978-1-4244-0922-8. doi:[10.1109/NSSMIC.2007.4437209](https://doi.org/10.1109/NSSMIC.2007.4437209).
- [55] C. N. Chou. The nature of the saturation effect of fluorescent scintillators. *Phys. Rev.*, 87:904–905, Sep 1952. doi:[10.1103/PhysRev.87.904](https://doi.org/10.1103/PhysRev.87.904). URL <https://link.aps.org/doi/10.1103/PhysRev.87.904>.